Journal of Power Sources 565 (2023) 232910

Contents lists available at ScienceDirect

Journal of Power Sources

journal homepage: www.elsevier.com/locate/jpowsour

Catenated pyrrolidinium-magnesium-organochlorostannate ionic liquid electrolytes for multivalent metal batteries

Gioele Pagot [a,b], Joy A. Kieser [a,c], Federico Brombin [a,b], Keti Vezzù [a,b], Juergen Janek [c], Vito Di Noto [a,b,*]

[a] Section of Chemistry for Technology, Department of Industrial Engineering, University of Padova, Via Marzolo 9, 35131, Padova, Italy
[b] National Interuniversity Consortium of Materials Science and Technology (INSTM), Florence, Italy
[c] Institute of Physical Chemistry, Justus-Liebig-University Gießen, Heinrich-Buff-Ring 17, 35392, Giessen, Germany

HIGHLIGHTS

- Ionic liquid electrolytes for secondary battery applications are proposed.
- Metal is depositing with low overpotential and good current density.
- Broadband electrical spectroscopy clarifies the conductivity mechanism.
- Complex catenated Mg-based anionic 3D networks are formed.

GRAPHICAL ABSTRACT

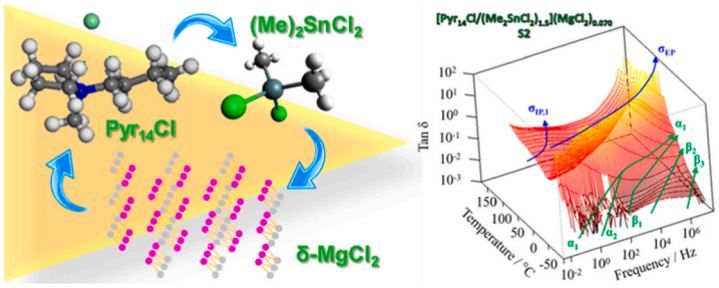

ARTICLE INFO

Keywords:
Ionic liquid electrolyte
Broadband electric spectroscopy
δ-$MgCl_2$
Magnesium battery
Organohalogenated tin complexes

ABSTRACT

The quest for the development of high performing secondary batteries is prompting the research activities in this field towards the exploitation of new cell concepts. In this concern, next-generation secondary batteries based on multivalent metals such as magnesium and tin are an important promise. In this report, a new family of multivalent metal-based ionic liquid (IL) electrolytes is developed. The proposed ILs are obtained by reacting 1-butyl-1-methylpyrrolidinium chloride ($Pyr_{14}Cl$), dimethyl-tin dichloride and the highly electroactive δ-$MgCl_2$ material. Thermal and vibrational spectroscopy studies reveal that the proposed electrolytes consist of domains of complex catenated 3D magnesium-organochlorostannate coordination networks neutralized by aggregates of Pyr_{14}^{+} stacks. The anionic domains are composed by a network of catenated $[Me_{2x}Sn_xCl_{2x+y}]^{y-}$ repeat units bonded by $MgCl_x$ bridges. Cyclic voltammetry studies reveal that the metal deposition and stripping processes occur with a low overpotential in the order of few tens of mV. Finally, broadband electrical spectroscopy studies show that these new IL electrolytes: (i) are characterized by a room temperature ionic conductivity in the order of 10^{-3} S cm^{-1}; and (ii) exhibit host matrix relaxations which are very effective in facilitating the long-range charge migration processes responsible for the overall conductivity of materials.

* Corresponding author. Section of Chemistry for Technology, Department of Industrial Engineering, University of Padova, Via Marzolo 9, 35131, Padova, Italy.
E-mail address: vito.dinoto@unipd.it (V. Di Noto).

https://doi.org/10.1016/j.jpowsour.2023.232910
Received 31 August 2022; Received in revised form 13 February 2023; Accepted 28 February 2023
Available online 7 March 2023
0378-7753/© 2023 Published by Elsevier B.V.

1. Introduction

The growing market of electric vehicles, and the increasing production of electrical energy from renewable sources, make secondary batteries strategic technologies to fulfil the European Union's clean and digital transition. Secondary batteries still face several challenges related to the performance, cost, availability of raw materials and recycling technology [1–3]. In this scenario, magnesium-based batteries offer a good alternative to the lithium technology, thanks to Mg high gravimetric and volumetric capacity (3862 Ah·kg^{-1} and 2062 Ah·dm^{-3} for Li *vs.* 2205 Ah·kg^{-1} and 3832 Ah·dm^{-3} for Mg), low reduction potential (-3.04 and −2.37 V *vs.* SHE for Li and Mg, respectively), high abundance in the Earth's crust and low cost (Mg is currently 24 times cheaper than Li) [1,4]. Although the magnesium battery technology has been demonstrated more than two decades ago [5–7], it is still at its scientific infancy. The main roadblock to its widespread use is the development of suitable electrolytes able to reconcile the electrochemistry of the battery electrodes (*i.e.*, the anode and the cathode) rising the efficiency of Mg deposition and stripping processes [8–10]. Indeed, Mg metal has the propensity to rapidly passivate growing a Mg^{2+}-based blocking surface [1,9], differently from the solid electrolyte interface typically formed in lithium and sodium batteries [11–15]. Mg deposition and plating redox processes can be obtained using Grignard or introducing Cl-based compounds such as $MgCl_2$ and $AlCl_3$ [1,9]. While these latter materials show a performance which is competing with that of Li-based organic electrolytes in terms of coulombic efficiency (*ca.* 99%) and ionic conductivity (*ca.* 10^{-3} S cm^{-1}), these electrolytes, which include highly volatile and/or highly flammable organic solvents, show a large overpotential in the deposition/stripping processes [1,4,9]. The volatility and flammability issues can be solved by developing polymeric [16–19], ceramic [20–22], and ionic liquid-based (IL) [8,23–26] Mg^{2+} conducting electrolytes. The IL electrolytes are able to deposit and strip a highly electroactive Mg metal layer at a very low overpotential (potential window <50 mV *vs.* Mg/Mg^{2+}) [23,27–29]. Therefore, they are very promising electrolytes for application in magnesium secondary batteries. An add-on of these IL electrolytes is the use of δ-$MgCl_2$ [16,17,30,31], a particular crystallographic polymorph of $MgCl_2$ which is characterized by a particular structure, a high structural disorder and a high reactivity. δ-$MgCl_2$ presents a nanoribbon structure with polymeric chains composed by planar $MgCl_2$ repeat units [32]. This particular structure plays a crucial role in modulating the complex coordination network formed in IL-based electrolytes [28,33].

Indeed, results elsewhere reported [23,29] demonstrate that the weak coordination of chloro-metalates with a distorted planar square coordination geometry of Mg atoms in a 3D network, allows: (i) to rise the density of magnesium chloride species and thus the conductivity of the electrolytes; (ii) to enhance the kinetics and the reversibility of Mg-deposition/stripping processes at the interface electrode-electrolyte [33]; and (iii) to promote the relaxations of the 3D network host matrix increasing the mobility of magnesium ion species.

In this report, a new class of IL electrolytes for application in magnesium secondary batteries is obtained by reaction between 1-butyl-1-methylpyrrolidinium chloride ($Pyr_{14}Cl$), δ-$MgCl_2$ and dimethyl-tin dichloride (Me_2SnCl_2). The aim is to foster in electrolytes: (i) the high stability and solvating ability of $Pyr_{14}Cl$; (ii) the high reactivity and solubility of δ-$MgCl_2$; and (iii) the ability of the Me_2SnCl_2 component to react with $Pyr_{14}Cl$ and δ-$MgCl_2$ species to yield 3D catenated network structures with Mg coordination geometries similar to that of δ-$MgCl_2$ [34,35]. In details, Me_2SnCl_2 is selected owing to its ability to coordinate weakly δ-$MgCl_2$ species to yield electrolytes with: (i) a high flexibility and mobility in dynamic 3D catenated host network structure; (ii) tin atoms linearly bonded to Mg in a planar distorted geometry by four chloride bridges [35] and with methyl groups out of the plane in a *trans* configuration [36]; and (iii) a large difference between the standard reduction potentials of tin and magnesium (*i.e.*, $\Delta E_{Sn\text{-}Mg} = 2.53$ V and $\Delta E_{Al\text{-}Mg} = 0.71$ V). This latter target is crucial in order to obtain, with respect to other similar electrolytes based on aluminum and magnesium [29], an electrodeposited alloy richer in magnesium.

The obtained new multi-metal IL electrolytes demonstrate: (i) a high room temperature ionic conductivity ($1.19{\cdot}10^{-3}$ S cm^{-1}); (ii) the ability at the anode half-cell to deposit and strip Mg metal with a low overpotential (<100 mV *vs.* Mg/Mg^{2+}) and a good current density (up to $60{\cdot}10^{-3}$ mA cm^{-2}); and (iii) an electrochemical stability window which extends up to 1.6 V *vs.* Mg/Mg^{2+}. One of the main targets of this study is to investigate how the host medium relaxations of the complex catenated 3D network structure of ILs are coupled with the long-range charge migration processes responsible of the overall conductivity of materials. Therefore, particular attention is also devoted in understanding: (i) the conduction mechanism specific for the proposed IL-based electrolytes; and (ii) the influence of the structure of the catenated 3D networks on the faradic phenomena taking place at the magnesium metal/electrolyte interface.

2. Experimental section

2.1. Reagents

$Pyr_{14}Cl$ was purchased from IoLiTec and dried under vacuum at 105 °C for 7 days. Metallic magnesium (50 mesh) and 1-chlorobutane were obtained from Sigma-Aldrich. Dimethyl-tin dichloride (Me_2SnCl_2) was purchased as reagent-grade from ABCr. 1-chlorobutane was further purified by standard methods and stored under Argon on 4 Å molecular sieves to prevent moisture contamination. Me_2SnCl_2 was dried under vacuum at room temperature for 3 days.

2.2. Preparation of IL-based electrolytes

Anhydrous δ-$MgCl_2$ salt was synthetized by direct reaction between magnesium powder and anhydrous 1-chlorobutane in reflux for 3 h under a constant flow of nitrogen gas using a Schlenk line. Further details can be found in Ref. [16]. The pristine IL (sample 0, S0) was prepared by slow addition of an appropriate amount of Me_2SnCl_2 to $Pyr_{14}Cl$. In order to synthetized a Lewis acidic IL, the final Pyr_{14} to Sn molar ratio was 1:1.5. The melt was kept under stirring for 48 h. This reaction was performed inside an Ar-filled glove box ($p(H_2O)/p < 1$ ppm, $p(O_2)/p < 1$ ppm). An IL solution saturated with δ-$MgCl_2$ (sample 3, S3) was prepared by slowly adding the magnesium salt into IL S0, until a solid precipitate was observed. The suspension was left under stirring for 4 days, and then the supernatant was extracted by centrifugation at 5′000 rpm. Intermediate concentration magnesium electrolyte solutions S1 and S2 were prepared by dilution of S3 with S0 at 1:1 and 1:3 vol ratio, respectively. The effective chemical composition of the four electrolytes, which present the general formula $[Pyr_{14}Cl/(Me_2SnCl_2)_{1.5}]/(\delta\text{-}MgCl_2)_x$ with $0 \leq x \leq 0.127$, was determined by means of inductively coupled plasma atomic emission spectroscopy (ICP SPECTRO Arcos). Results of elemental ultra-trace analyses in the instrumental detection limit up to 1 ppb, carried out on the four proposed electrolytes, are reported in Table S1 of the Supporting Information. These show that, except Sn and Mg, the only element revealed in samples is Zn, which exhibits a concentration of *ca.* $6.8{\cdot}10^{-3}$ %wt. No other elements (*i.e.*, Al, As, B, Ba, Ca, Cd, Co, Cr, Cu, Fe, Hg, Li, Mn, Na, Ni, P, Pb, Sb, Se, Si, Sr, Ti, V and Zr) are detected in the above average instrumental detection limit. The purity of electrolytes is then finalized checking in samples the complete elimination of solvents and water traces by vibrational spectroscopy (see FT-MIR spectra reported in Fig. S1 of the Supporting Information). All storage and manipulations of electrolytes were carried out under a strictly inert atmosphere inside a glove-box.

2.3. Thermal behavior

The thermal properties of $[Pyr_{14}Cl/(Me_2SnCl_2)_{1.5}]/(\delta\text{-}MgCl_2)_x$ were

determined by means of modulated differential scanning calorimetry investigations (MDSC) using a MDSC Q20 instrument (TA Instruments) equipped with a liquid nitrogen cooling system. Measurements were carried out using a heating ramp of 3 °C min^{-1} in the temperature range from −130 to +150 °C. Each sample was hermetically sealed into an aluminum pan inside a glovebox.

2.4. Vibrational studies

The structure and the interactions characterizing the complex 3D network of the proposed materials were investigated by means of FT-IR vibrational spectroscopy in both the medium (4000 - 400 cm^{-1}) and far (600 - 50 cm^{-1}) infrared regions. Mid FT-IR spectra were collected with a diamond attenuated total reflectance (ATR) cell using a Thermo Scientific™ Nicolet™ iS50 instrument. Far FT-IR studies were performed in transmittance mode, sealing the samples between two polyethylene windows and using a Nicolet FT-IR Nexus spectrometer. First-principles-based electronic structure calculations were carried out using the DMol3 package in Materials Studio software. The density functional theory (DFT) computations were performed selecting the BLYP functionals with the GGA basis set.

2.5. Electrochemical studies

The electrochemical properties of the IL electrolytes were studied by means of cyclic voltammetry (CV) experiments in a three-electrode cell, using Pt as working electrode (WE) and two Mg ribbons as counter (CE) and reference (RE) electrodes. CV profiles were acquired at a scan rate of 20 mV s^{-1} in the potential range between −0.3 and + 0.5 V *vs.* Mg/Mg^{2+}. The electrochemical stability window (ESW) was determined by means of linear sweep voltammetry (LSV) measurements performed at a scan rate of 5 mV s^{-1}. All the electrochemical measurements were executed at room temperature using a VMP-300 potentiostat/galvanostat instrument of Bio-Logic. A potentiostatic electrodeposition was performed on a Pt working electrode using the $[Pyr_{14}Cl/(Me_2SnCl_2)_{1.5}]/(\delta\text{-}MgCl_2)_{0127}$ electrolyte (S3) and applying −0.3 V *vs.* a Mg^{2+}/Mg reference electrode for 20 min at T = 25 °C. The residual electrolyte on the deposited layer was removed by rinsing the Pt electrode for three times with ultra-dry toluene. The electrodeposited layer was then analyzed by means of a JEOL JSM 7900F HR-FEG-SEM. An accelerating voltage of 15 kV was applied during the measurements. The EDS elemental analysis was performed by means of an Oxford Instrument ULTIM MAX 40 probe.

2.6. Electric response

The electric response of the IL-based electrolytes was studied using a Novocontrol Alpha-A analyzer in the frequency range from 30 mHz to 10 MHz and in the temperature range between −110 and 100 °C. The temperature was controlled using a homemade cryostat operating with an N_2 gas jet heating and cooling system. The temperature was measured with an accuracy greater than ±0.2 °C. Few drops of each sample were sandwiched between two circular platinum electrodes (13 mm of diameter), using glass fibers with a diameter of 125 μm as spacers. The final distance between the electrodes was determined by using a micrometer. The whole system was hermetically sealed inside a homemade Teflon cell under Argon atmosphere and maintained under nitrogen during the measurements.

3. Results and discussion

3.1. Stoichiometry and thermal properties

The composition of the $[Pyr_{14}Cl/(Me_2SnCl_2)_{1.5}]/(\delta\text{-}MgCl_2)_x$ electrolytes with *x* ranging from 0 to 0.127 was determined by means of ICP-AES measurements. Results are summarized in Table 1.

Table 1
Composition of $[Pyr_{14}Cl/(Me_2SnCl_2)_{1.5}]/(\delta\text{-}MgCl_2)_x$ electrolytes.

sample	IL (wt%)	δ-$MgCl_2$ (wt%)	x[a]	z[b]
S0	100	0	0	∞
S1	99.34	0.66	0.036	41.7
S2	98.72	1.28	0.070	21.4
S3[c]	97.70	2.30	0.127	11.8

[a] x is the ratio between the moles of magnesium (n_{Mg}) and the moles of the Ionic Liquid (n_{IL}). The molecular repeat unit structure of IL is $[Pyr_{14}Cl/(Me_2SnCl_2)_{1.5}]$ (MW_{IL} = 507.245 g mol^{-1}).
[b] $z = n_{Sn}/n_{Mg}$. n_{Sn} and n_{Mg} are the moles of tin and magnesium, respectively in the ionic liquid.
[c] Saturated solution.

The thermal properties of the proposed electrolytes were investigated by MDSC measurements. Results reported in Fig. 1 show the presence of three thermal events: (a) a glass transition (T_g) at *ca.* −47 °C; (b) an exothermic crystallization event (T_c) at *ca.* 0 °C for samples with $x \geq 0.036$; and (c) a melting transition (T_m) at *ca.* 10 °C. In accordance with other studies [37,38], these thermal events can be easily attributed assuming that the IL electrolytes: (i) consist on the mesoscale of anionic and cationic nanodomains; and (ii) present in the anion nanodomains a well-defined catenated 3D network structure. As expected, the Pyr_{14}^+ cation aggregates and this dynamic catenated 3D network can re-arrange on temperature, assuming different mesoscale morphologies. These are likely triggered by the interactions and the metal coordination geometries assumed by the material repeat units [39–41]. On this basis, and if we consider that the T_g transition (phase I → II, Fig. 1b) is not influenced by the concentration of δ-$MgCl_2$ in electrolytes, it is easy to associate this event to an order-disorder transition involving the pyrrolidinium cation aggregates neutralizing the rigid organochlorostannate catenated 3D network [23,33]. These results, which are in accordance with other studies [23,33], suggest that magnesium chloride units are coordinated in anionic domains by the anion organochlorostannate repeat units of the IL, and that this type of interactions at this temperature are only marginally affecting the structure of the Pyr_{14}^+ cation aggregates reorganized in stacks. Similarly to imidazolium-based ILs [23,27], also in this case a T_c (phase II → IIa, Fig. 1b) is revealed, which is assigned to a typical structural reorganization of Pyr_{14}^+ cations along the stacking axis of the pillars. Actually, T_c is assigned to a thermal transition from an ordered pillar of Pyr_{14}^+ cations to another one with Pyr_{14}^+ cations reorganized along the stack axis in a zig-zag structure [23]. Interestingly, this thermal event, which is observed only when δ-$MgCl_2$ component is present into the electrolytes (*i.e.*, at $x \geq 0.036$), depends on *x*. This corroborates the hypothesis that the particular crystallographic form of δ-$MgCl_2$ facilitates the interactions with organochlorostannate anion ligands stabilizing and raising the size of the anionic domains of IL electrolytes [28]. These stabilized anionic domains weaken the electrostatic interactions with cation aggregates, improving their bulk charge delocalization and facilitating the transition in cation aggregates [28]. T_m is attributed to the melting transition of the electrolytes (phase IIa → III, Fig. 1b). Like T_c, also T_m depends on the magnesium concentration, indicating that in the electrolytes the structural features of anion clusters strongly affect the temperature of this thermal event. Taken all together, MDSC studies confirm that, at the mesoscale, these IL electrolytes consist of Pyr_{14}^+ cations, organized in aggregates of stacks, which are neutralizing the negative charges present along the 3D network structure of catenated [organochlorostannate-$MgCl_x$] repeat units. These structural features are the consequence of the typical planar polymeric structure of δ-$MgCl_2$, which is very effective in stabilizing the network of 3D-catenated anionic metal species of electrolytes.

3.2. Vibrational studies

The FT-IR spectroscopy studies in the medium and far infrared

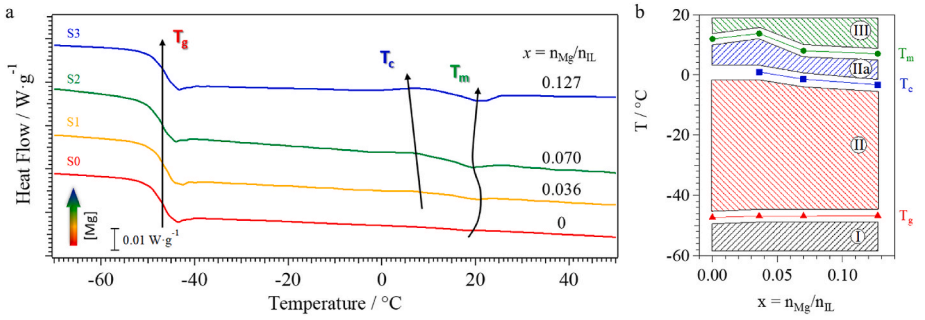

Fig. 1. MDSC profiles of electrolytes on x: $x = 0$ (S0, red), 0.036 (S1, yellow), 0.070 (S2, green), and 0.127 (S3, blue) (a). Thermal events shown corresponds to a glass transition (T_g), a crystallization transition (T_c), and a melting transition (T_m). Phase diagram *vs.* $x = n_{Mg}/n_{IL}$ of $[Pyr_{14}Cl/(Me_2SnCl_2)_{1.5}]/(\delta\text{-}MgCl_2)_x$ IL electrolytes (b). Thermal events are identified by a different color and marker: T_g (red triangles), T_c (blue squares) and T_m (green circles). The phases are indicated with roman numbers from "I" to "III". (For interpretation of the references to color in this figure legend, the reader is referred to the Web version of this article.)

regions were carried out to identify the molecular structure and the interactions present in IL electrolytes. Fig. S2 of the Supporting Information show the FT-MIR spectra of the $[Pyr_{14}Cl/(Me_2SnCl_2)_{1.5}]/(\delta\text{-}MgCl_2)_x$ samples on x. A detailed correlative assignment of the spectra is summarized in Table S2 of the Supporting Information. In order to confirm and fully assign the experimental spectral features summarized in Table S2, a number of possible [organochlorostannate-$MgCl_x$] repeat units were studied by DFT calculations. A careful analysis of the FT-IR spectra shows that in the medium infrared region the spectra: (i) are dominated by the vibrational modes of the Pyr_{14}^+ cation [29,42–48]; and (ii) are independent on x. Indeed, no changes on x of the number of modes, peak shape and position are observed. This is in agreement with the hypothesis that $MgCl_x$ moieties are coordinated by the catenated repeat units of the anionic 3D network domains of the IL, which affect only marginally the vibrational modes of the Pyr_{14}^+ cation aggregates. Differences in intensity are observed only below 860 cm^{-1}, where intense vibrational modes attributed to the organochlorostannate species are present. In particular, the bands peaking at *ca.* 793 and 739 cm^{-1} correspond to the rocking (ρ) and wagging (ω) vibrational modes of CH functionalities of organochlorostannate repeat units, respectively [45,49]. The Sn–Cl and Sn–C stretching vibrations are observed at *ca.* 565 and 517 cm^{-1}, respectively [36,45,49,50]. With respect to the electrolytes with $x \geq 0.036$, in S0 (*i.e.*, in the sample in absence of δ-$MgCl_2$) these peaks are more intense. This suggests that -($MgCl_x$)- species in bulk electrolytes contribute to stabilize and to increase the density of Mg-bridges between organochlorostannate species in catenated anionic 3D networks. In particular, the coordination of $MgCl_x$ species in anionic domains of materials by organochlorostannate repeat units acts to reduce the density of Sn-X (X = –CH_3, -Cl) coordination bonds.

To obtain more insight on the metal-ligand structure and interactions in electrolytes (*i.e.*, Mg–Cl, Sn–Cl coordination bonds), far FT-IR spectra were acquired and studied. Results are shown in Fig. 2a. The assignments of the observed vibrational modes were at first performed correlatively on the basis of literature data, and secondly confirmed and completed by DFT calculations. This study allows to identify in anionic domains of the electrolytes different organochlorostannate repeat units with a general formula $[Me_{2x}Sn_xCl_{2x+y}]^{y-}$. Selected representative structural models are briefly shown in Fig. 2b. In accordance with other studies [51], DFT investigations demonstrate that the most representative organochlorostannate model to describe the anionic domains are: the $[Me_2SnCl_3]^-$ monomeric and the $[Me_4Sn_2Cl_5]^-$ dimeric repeat units. It is also revealed that the above described monomer and dimer forms can easily interact to yield the less probable $[Me_6Sn_3Cl_8]^{2-}$ trimer. It should be noticed that the Sn–Cl stretching vibrational mode of the monomer form shifts to higher wavenumbers in the dimer. This

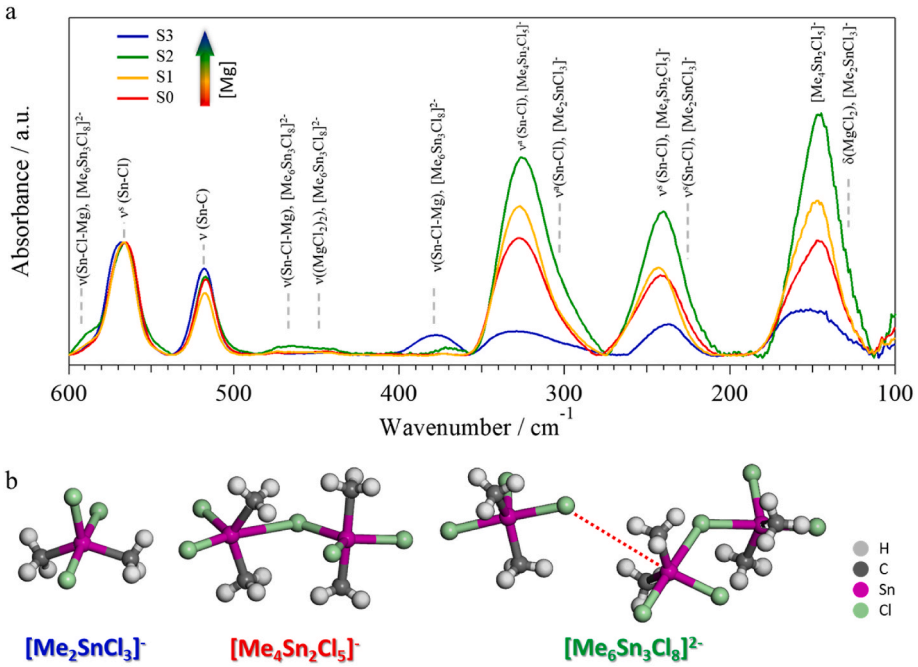

Fig. 2. Far-FT-IR spectra of IL electrolytes on x: $x = 0$ (S0, red), 0.036 (S1, yellow), 0.070 (S2, green), and 0.127 (S3, blue) (a). The assignment of vibrational modes is shown in the figure. Organochlorostannate model complexes studied by DFT calculation (b). Color legend: hydrogen (grey), carbon (black), tin (violet) and chlorine (green). (For interpretation of the references to color in this figure legend, the reader is referred to the Web version of this article.)

demonstrates that the strength of the Sn–Cl bond in organochlorostannate repeat units increases going from the monomer to the dimer form. On *x*, the intensities attributed to the dimer species increase, indicating that the addition of δ-$MgCl_2$ in electrolytes favors the formation of dimeric $[Me_4Sn_2Cl_5]^-$ chemical species. This is a further confirmation of the ability of δ-$MgCl_2$ to promote and stabilize the catenated 3D networks characterizing the anionic domains of proposed IL electrolytes. The interactions between the monomer and the dimer forms to yield the $[Me_6Sn_3Cl_8]^{2-}$ trimer species are supported by the three weak peaks centered at *ca.* 590, 470 and 440 cm^{-1}. The presence of $MgCl_x$ species is evidenced by the peaks appearing at *ca.* 440, 370 and 145 cm^{-1}, which are assigned to the Sn–Cl–Mg stretching vibrations [23,29]. In particular, the peaks present at *ca.* 590, 470, 440 and 370 cm^{-1}, which are attributed to metal-chloro-magnesium stretching vibrational modes [23,29], indicate that chlorine atoms act as bridges between different metal ions yielding a 3D anionic network. The formation of direct Sn–Sn and Sn–Mg bonds is excluded by the absence of the corresponding vibrational modes expected at *ca.* 190 cm^{-1} [52]. Taken all together, vibrational studies: (i) confirm the above structural hypotheses, showing that in electrolytes $MgCl_x$ units are interacting with organochlorostannate ligands forming catenated anionic domains; and (ii) demonstrate that these IL electrolytes conduct owing to the migration of electrochemically active species, which are confined in anionic catenated 3D network domains.

3.3. Electrochemical studies

The electrochemical performance of the proposed electrolytes was investigated by means of cyclic voltammetry experiments (Fig. 3 and Fig. S3 in the Supporting Information). Two redox events are observed in the CV profiles. In the negative potential sweep, the electrochemical reduction of Mg^{2+} and Sn^{4+} at *ca.* 60 mV *vs.* Mg/Mg^{2+} is observed. This event is attributed to the electrodeposition of the metals or of their alloys onto the Pt working electrode. In the anodic sweep, a metal oxidation event is revealed at *ca.* 10 mV *vs.* Mg/Mg^{2+}. This corresponds to the stripping of the deposited metals during the positive sweep process. As elsewhere demonstrated [23,27–29], the electrodeposited layer from IL electrolytes in general consists of magnesium alloys with different metals. The electrolytes here developed show redox processes with a narrow potential window of few tens of mV (<100 mV *vs.* Mg/Mg^{2+}).

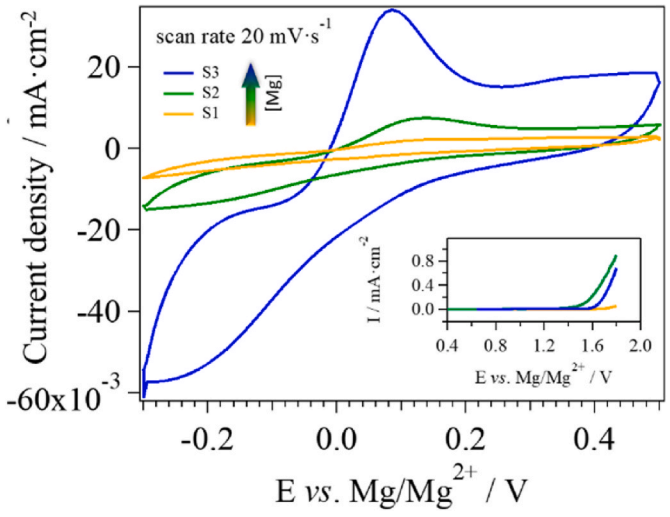

Fig. 3. Cyclic voltammetry studies of $[Pyr_{14}Cl/(Me_2SnCl_2)_{1.5}]/(\delta\text{-}MgCl_2)_x$ on *x*, with $x \geq 0.036$. Measurements are carried out in a three electrodes cell at a scan rate of 20 mV s^{-1}. The working, counter and reference electrode is Pt, Mg foil, and Mg ribbon, respectively. The inset shows the electrochemical stability window of the IL electrolytes determined by linear sweeping voltammetry measurements at a scan rate of 5 mV s^{-1}.

This makes the proposed electrolytes very promising for application in secondary Mg batteries. Interestingly, the current density of electrodeposition and dissolution raises on *x*, thus indicating that the formation of anionic 3D catenated networks including $MgCl_x$ species improves the electrochemical performance of the electrolytes. In addition, the shape and the intensity of observed CV peaks are: (i) broader and less intense with respect to those obtained from Al-based IL electrolytes [29]; and (ii) similar to those exhibited by Ti-based IL electrolytes [28]. Likely, Ti- and Sn-based electrolytes, which are both characterized by a complex chemistry, have some similarities in promoting the growing of an extended anionic catenated 3D network in the electrolytes [28,35,53,54]. The latter is responsible for the high electroactivity of the electrolyte.

Taken all together, CV experiments demonstrated that the targets described in the introduction are achieved. Indeed, in CV measurements, anionic catenated 3D networks give rise to a reversible deposition and stripping process yielding a Sn/Mg alloy deposit richer in Mg. This is likely possible owing to the weak coordination interactions characterizing the 3D co-catenated networks based on Mg^{2+} and Sn^{4+} ions bonded together through Cl^- bridges in a planar distorted coordination geometry which, as expected, facilitates the kinetics of metal ion reduction and deposition processes at the electrode-electrolyte interface (see Fig. 3 and Fig. S3 in the Supporting Information). These results are in accordance with those of similar electrolytes based on Ti and Al species [28,29].

In addition, the ability of proposed electrolytes to deposit Sn/Mg alloys richer in Mg with respect to that formed using Al-based ILs was proved by a SEM-EDS analysis carried out on a layer obtained by a potentiostatic electrodeposition of the alloy on a Pt electrode (see Fig. S4 of the Supporting Information). Results shows that Mg and Sn are homogeneously distributed in the alloy, which exhibits a Sn/Mg molar ratio of 2.2:1. It should be highlighted that this molar ratio is at least 5 times higher in Mg than that of the pristine electrolyte (see z value in Table 1) where the Sn/Mg molar ratio ranges between 11.8 and 41.7. A comparison of these results with those of the deposits obtained by similar Al-based IL electrolytes [29], which yield alloys with an Al/Mg molar ratio of 10.5:1, confirms that in order to obtain an electrodeposited alloy richer in magnesium it is necessary to use electrolytes based on a co-metal such as Sn, with a far greater reduction potential with respect to Mg.

Finally, the proposed IL electrolytes show an electrochemical stability window which extends up to *ca.* 1.6 V *vs.* Mg/Mg^{2+} (inset of Fig. 3). Actually, the stability in the anodic sweep is limited by the oxidation of chloride species which at high potential are oxidized to chlorine.

3.4. Electrical studies

The electric response of the $[Pyr_{14}Cl/(Me_2SnCl_2)_{1.5}]/(\delta\text{-}MgCl_2)_x$ electrolytes was studied carefully by means of the broadband electrical spectroscopy (BES). The BES technique is useful to determine and study the polarization and dielectric relaxation events of materials. In particular, it permits to elucidate the conduction mechanism of electrolytes and to shed light on the correlations between the structure, composition and the electric response of ion-conducting materials [55–59]. Here, this aim is pursued by studying the electric response of IL electrolytes on temperature and δ-$MgCl_2$ doping. The 3D *tan δ* spectra of the proposed electrolytes are shown in Fig. 4. A comparative qualitative analysis of profiles of real and imaginary components of complex conductivity and permittivity spectra of samples allowed to detect one electrode polarization (σ_{EP}) and up to three interdomain polarization ($\sigma_{IP,i}$, with $1 \leq i \leq 3$) events (see Fig. 4). σ_{EP} corresponds to the accumulation of charges at the electrode/electrolyte interfaces, while $\sigma_{IP,i}$ are attributed to the accumulation of charges at the interfaces between domains with different permittivity in bulk electrolytes. The presence of $\sigma_{IP,i}$ indicates that the electrolytes in the mesoscale are characterized by

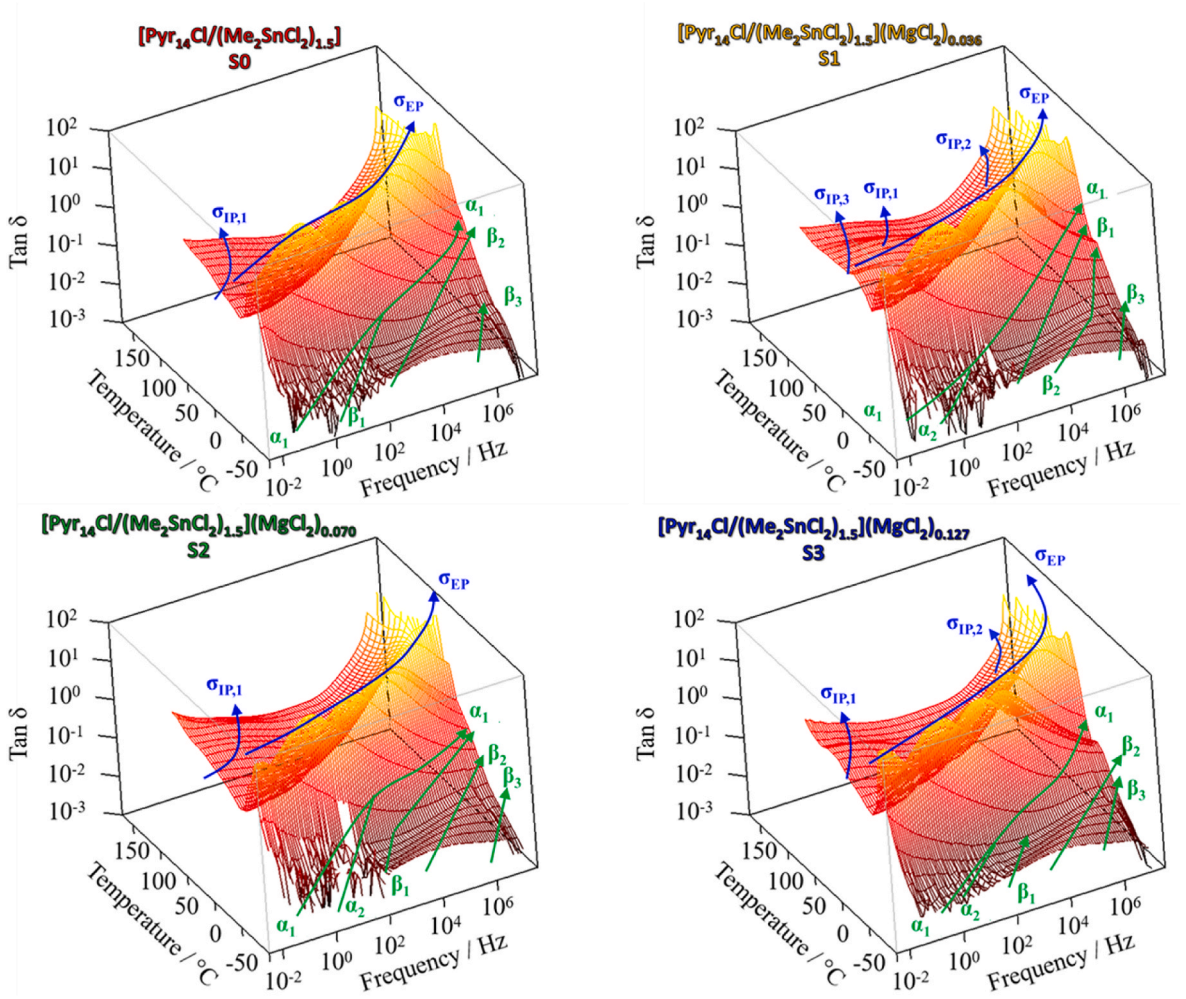

Fig. 4. 3D tan δ spectra as a function of frequency and temperature of the $[Pyr_{14}Cl/(Me_2SnCl_2)_{1.5}]/(\delta\text{-}MgCl_2)_x$ samples. Polarization phenomena and dielectric relaxation events are highlighted in blue and green colors, respectively. (For interpretation of the references to color in this figure legend, the reader is referred to the Web version of this article.)

nano-heterogeneities. Furthermore, in the high frequency wing of spectra at low temperature up to two α_i and three β_i dielectric relaxations are revealed (see Fig. 4). For the sake of completeness, in Figs. S5–S8 of the Supporting Information is reported on temperature and frequency the electric response of each sample, in terms of its real and imaginary component of complex permittivity (ε' and ε'') and conductivity (σ' and σ'') spectra. The electric response of samples on temperature and composition is studied quantitatively as elsewhere described [55,60], by fitting ε', ε'', σ', σ'', and tan δ representations simultaneously by Equations 1 and 2:

$$\varepsilon_m^*(\omega) = -i\left(\frac{\sigma_0}{\omega\varepsilon_0}\right)^N + \sum_{k=1}^{n}\frac{\sigma_k(i\omega\tau_k)^{\gamma_k}}{i\omega\varepsilon_0[1+(i\omega\tau_k)^{\gamma_k}]} + \sum_{j=1}^{m}\frac{\Delta\varepsilon_j}{\left[1+(i\omega\tau_j)^{a_j}\right]^{b_j}} + \varepsilon_\infty \quad (1)$$

and

$$\sigma^*(\omega) = i\omega\varepsilon_0\varepsilon^*(\omega) \quad (2)$$

The first term of Equation (1) is related to the material's conductivity at zero frequency (σ_0). ε_∞ corresponds to the permittivity of the material at infinite frequency (the electronic contribution). The second term accounts for the electrode and the interdomain polarizations. σ_k and τ_k are the conductivity and the relaxation time parameters, respectively, of the kth polarization event. γ_k is a parameter which takes into consideration the peak broadening of the kth polarization. The third term describes the dielectric relaxation events of the electrolytes [55,60]. $\Delta\varepsilon_j$, τ_j, α_j, and β_j are the dielectric strength, relaxation time, symmetric and antisymmetric shape parameters of the jth dielectric relaxation phenomenon, respectively.

3.4.1. Polarization phenomena

σ_{EP} and $\sigma_{IP,i}$ (with $1 \le i \le 3$) parameters and electric relaxation frequencies, determined as above described by fitting $\sigma^*(\omega)$ and $\varepsilon^*(\omega)$ complex spectra by Equations (1) and (2), are plotted vs. T^{-1} in Fig. 5a and b, respectively. σ_{EP} and $\sigma_{IP,i}$ are the different conductivity pathways of bulk materials which are contributing to the overall conductivity (σ_T) of electrolytes.

$$\sigma_T = \sigma_{EP} + \sum_{i=0}^{3}\sigma_{IP,i} \quad (3)$$

The presence of up to three $\sigma_{IP,i}$ conductivity pathways confirms that the electrolytes are heterogeneous on the mesoscale. This heterogeneity is originated by the presence in bulk materials of Pyr_{14}^+ cation aggregates neutralizing catenated anionic domains. The analysis of the σ_{EP} and $\sigma_{IP,i}$ curves on temperature shows three different temperature regions (I → III), which are delimited by the thermal events revealed by MDSC studies (T_m, T_c, T_g, see Paragraph 3.1). At $T > T_g$, four polarization phenomena are observed: (i) an intense electrode polarization (σ_{EP}) [33,55]; and (ii) three interdomain polarizations ($\sigma_{IP,i}$, with $1 \le i \le 3$) events [33,55]. Below the T_g (region I) only σ_{EP} is significantly contributing to

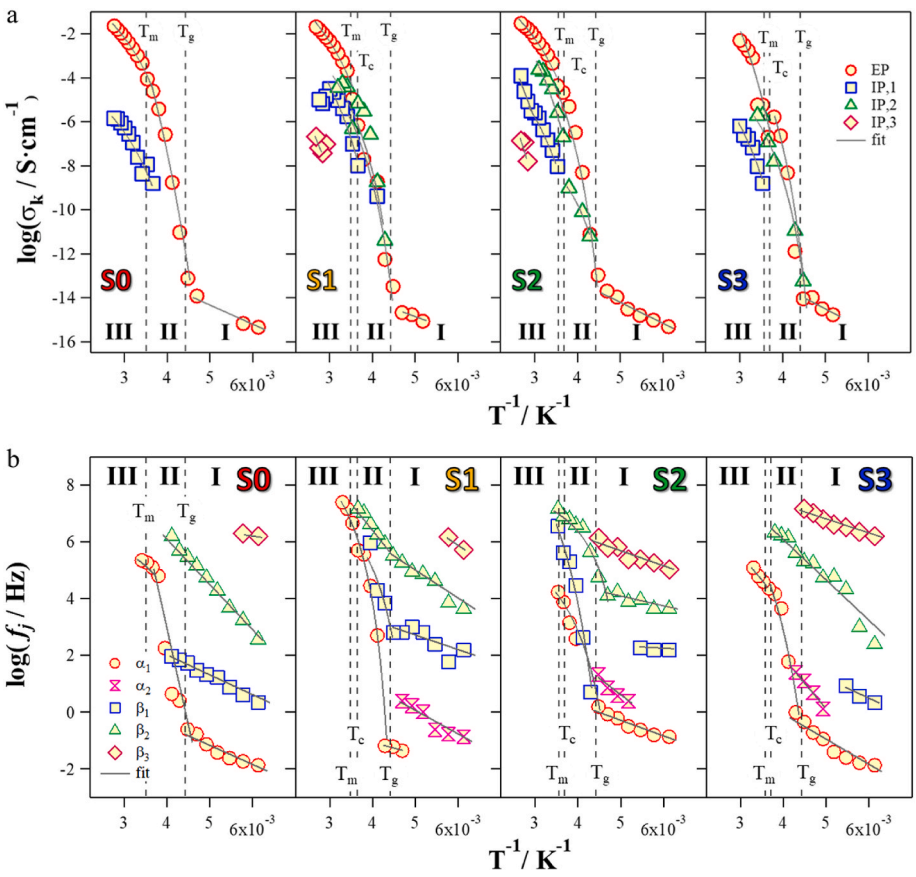

Fig. 5. Log σ_k vs. T^{-1} (a) and Log f_j *vs.* T^{-1} (b) for the $[Pyr_{14}Cl/(Me_2SnCl_2)_{1.5}]/(\delta\text{-}MgCl_2)_x$ samples. f_j is the frequency of dielectric relaxation phenomena. Three temperature regions are detected (I to III) which are delimited by the thermal transitions revealed by MDSC measurements.

the overall conductivity of the samples ($\sigma_T = \sigma_{EP} + \sum_{i=0}^{3}\sigma_{IP,i} \cong \sigma_{EP} < 10^{-14}$ S cm^{-1}). In this temperature region, σ_{EP} vs. T^{-1} exhibits an Arrhenius-like behavior, indicating that the long-range charge migration processes occur owing to charge exchange phenomena by hopping processes between different coordination sites present in catenated anionic domains. No contribution of the host IL matrix relaxations to the overall conductivity is observed. Above the T_g (regions II and III), $\sigma_{IP,i}$ start contributing significantly to the overall conductivity of the materials. This suggests that in II and III the relaxation modes of Pyr_{14}^+ cation aggregates and of the complex catenated anionic 3D networks are coupled with the long-range charge migration processes, thus contributing to the overall conductivity through the different percolation pathways. It is interesting to observe that a large number of interdomain polarization pathways ($\sigma_{IP,i}$) are present in electrolytes after their doping with δ-$MgCl_2$. This is a convincing proof that: (i) in bulk electrolytes the presence of $MgCl_x$ species acts to extend the 3D catenated complex anion network which owing to its complexity yields different conductivity pathways; and (ii) δ-$MgCl_2$ plays a crucial role in modulating the organochlorostannate dimer/monomer equilibrium and structure, thus affecting the intensity and relaxation modes of the $\sigma_{IP,i}$ phenomena. In addition, at $T > T_g$ (regions II and III), all the σ_k polarization events show vs. T^{-1} a VTF-like behavior, thus witnessing that the α relaxation modes of Pyr_{14}^+ cation aggregate domains are coupled with the relaxation modes of the catenated anionic 3D networks. Therefore, these relaxation modes modulate and facilitate the long-range charge migration processes in σ_k conductivity pathways. The dependence on T^{-1} of the overall conductivity (σ_T) of proposed samples is shown in Fig. 6. The major differences in conductivity values are observed when the electrolytes are at a temperature below T_g. In correspondence of T_c, in region II (Fig. 6), a drop of conductivity is registered, which increases as the concentration of $MgCl_x$ species in bulk electrolytes are rising. In the

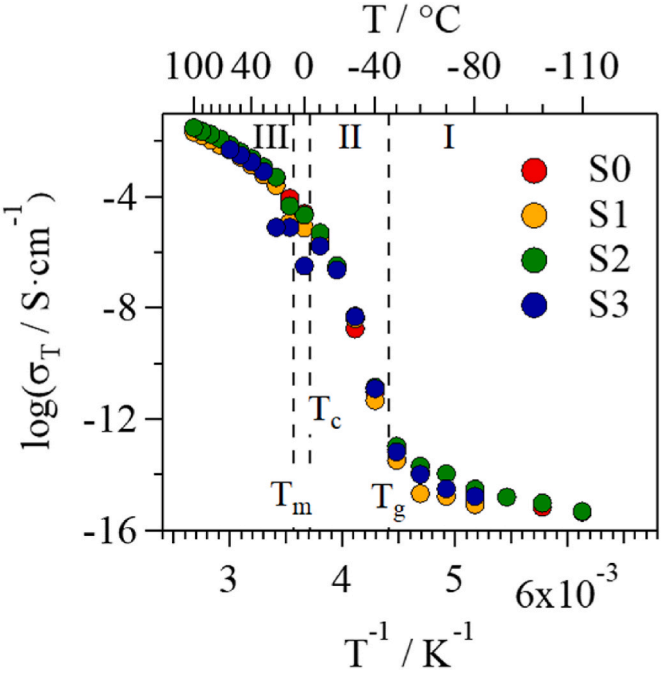

Fig. 6. Log σ_T vs. T^{-1} curves for the $[Pyr_{14}Cl/(Me_2SnCl_2)_{1.5}]/(\delta\text{-}MgCl_2)_x$ electrolytes. Regions I to III are delimited by the temperatures of thermal transitions detected by MDSC measurements.

sample at the highest δ-$MgCl_2$ concentration (S3), this drop of

conductivity is of at least two orders of magnitude. This evidence is in agreement with other studies on similar electrolytes and confirms that in bulk electrolytes the presence of catenated anionic 3D networks influences the structural transitions and the conduction mechanisms of samples. At room-temperature, S2 sample shows the highest ion conductivity value (*ca.* $1.19{\cdot}10^{-3}$ S cm^{-1}).

3.4.2. Dielectric relaxation events

To investigate the dielectric response of the electrolytes, the dependence of f_j on T^{-1} is studied (Fig. 5b). Below T_g, five dielectric relaxation events (f_j, with $1 \leq j \leq 5$) are observed: α_1-, α_2-, β_1-, β_2-and β_3-modes. In agreement with the literature [33], the β relaxations are assigned to the rotational motions of Pyr_{14}^+ cations as follows: (i) β_1, which is detected in the low frequency region, is attributed to the rotational motions around the short axis of rod-like Pyr_{14}^+ cations; (ii) β_2, which is detected in the medium frequency region, corresponds to the rotational motions around the long axis of Pyr_{14}^+ cations; and (iii) β_3, which is detected in the high frequency region, is attributed to the librational motions on the Pyr_{14}^+ ring plane. Sample S0 shows one α relaxation. This mode in the samples doped with δ-$MgCl_2$ is split into two dielectric relaxations α_1 and α_2, which, as expected, at $T > T_g$ shows a Vogel-Tammann-Fulcher-Hesse behavior (VTFH). This witnesses that the latter dielectric relaxations are associated to α modes. As expected, the α dielectric relaxations are detected at lower frequencies with respect to the β events. Indeed, the α-modes are associated to the diffusion of rotational motions of Pyr_{14}^+ units along the cation stacks, while β-modes are attributed to the local rotational relaxations of a single Pyr_{14}^+ molecule around a reference axis. In samples doped with δ-$MgCl_2$, the α relaxations are associated to the diffusion of rotational states along the pillar axis of two different pyrrolidinium cationic nanoaggregates [33]. After doping S0 with δ-$MgCl_2$, the splitting of α mode demonstrates that different interactions between cationic and anionic 3D catenated domains occur in electrolytes. In details, when $MgCl_x$ species are coordinated by organochlorostannate repeat units, slightly different electrostatic interactions between Pyr_{14}^+ cation aggregates and 3D anionic catenated domains are expected in electrolytes. These differences are easily revealed below T_g, *i.e.*, when the electrolytes are in an ordered structural reorganization, while are undistinguishable at $T > T_g$. The value of the frequency of each α-mode is a diagnostic index for studying the strength of electrostatic interactions characterizing the bulk structure of the electrolytes.

3.4.3. Activation energies of polarization and dielectric relaxation phenomena

To determine the activation energies (E_a) of conductivity pathways and dielectric relaxations, the curves of σ_k and f_j on T^{-1} (Fig. 5) are fitted by Arrhenius- or a VTF-like equations for σ_k, while by Arrhenius- or VTFH-like equations for f_j [55,61,62]. Results allow to clarify the correlation existent in materials between the dielectric relaxation events and the polarization phenomena. The study of these correlations sheds light on the influence of the dynamics of the anionic 3D catenated networks and of the Pyr_{14}^+ stack aggregates to the conduction mechanisms of electrolytes. To reveal these correlations, it is convenient to analyze carefully the activation energy correlation map shown in Fig. 7. In particular, in this map an activation energy of a dielectric relaxation event ($E_{a,fj}$) is correlated to an activation energy of a polarization phenomenon ($E_{a,\sigma k}$). The closer the marker is to the dashed diagonal line, the better σ_k correlates with the dielectric relaxation f_j. In these conditions, σ_k and f_j phenomena have a similar activation energy. Therefore, they are coupled to each other in triggering the long-range charge migration processes that modulate the conductivity of electrolytes. At a first view, the correlation map reveals a complex situation, which on the other hand is expected on the basis of the complex chemistry of electrolytes. However, a careful analysis of this map permits to demonstrate that, at low T (region I and II), both α and β dielectric relaxations are coupled to charge transfer phenomena of σ_{EP} and $\sigma_{IP,i}$ conductivity

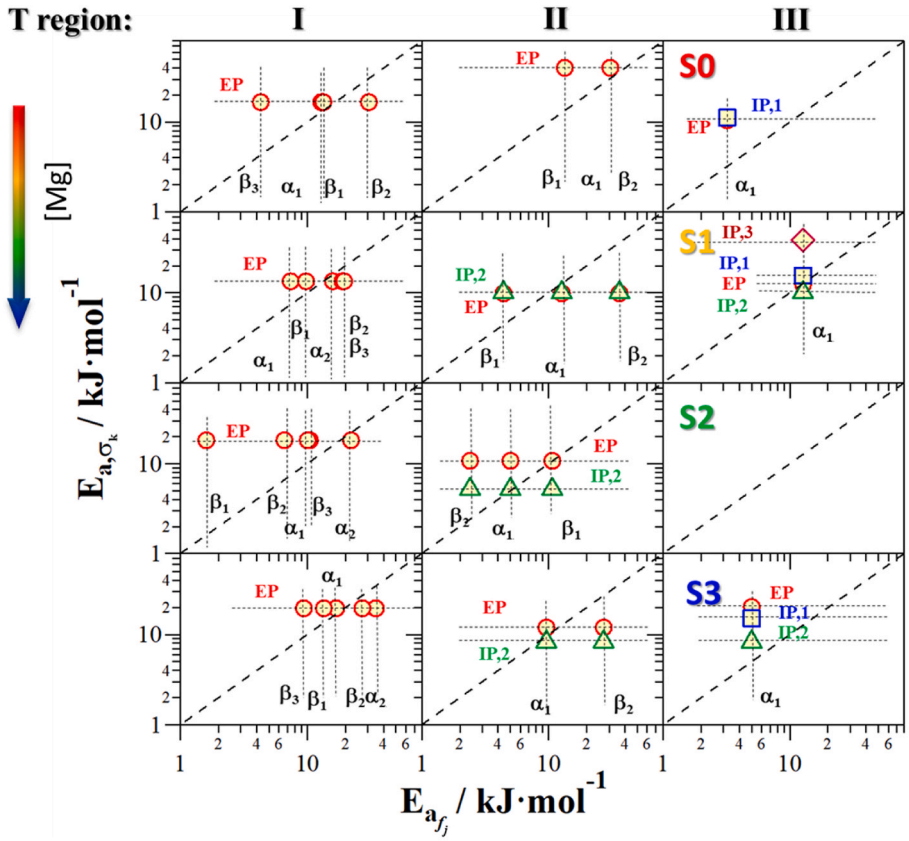

Fig. 7. Activation energy correlation map of dielectric (f_j) and polarization (σ_k) conductivity of investigated materials. Rows indicate the sample composition (*i.e.*, S0, S1, S2 and S3). Columns describe the different temperature regions (T increases in the order I → III). Horizontal and vertical dotted lines show the correlations between polarization and the dielectric relaxation events, respectively. Red circles are referred to σ_{EP}; blue squares to σ_{IP1}; green triangles to σ_{IP2}; and violet diamonds to σ_{IP3}. Dashed lines indicate the expected ideal correlation between polarization and dielectric relaxation phenomena. (For interpretation of the references to color in this figure legend, the reader is referred to the Web version of this article.)

pathways. At high T (region III), the diffusion of rotational states of Pyr_{14}^{+} units along the stacking axis (*i.e.*, α relaxations) is coupled with the activation energy values of conductivity pathways of electrolytes. These coupling effects seem to be more effective for samples with a lower concentration of $MgCl_x$ species. This suggests that a higher concentration of $MgCl_x$ species in electrolytes increases the rigidity of the 3D anionic catenated networks. Above T_g, and in particular in region II, it can be observed that the introduction in electrolytes of δ-$MgCl_2$ acts to reduce the values of the activation energies of both polarization phenomena and dielectric relaxation events. This allows to conclude that the electrostatic interactions between anionic 3D catenated networks and Pyr_{14}^{+} cation aggregates play a crucial role in modulating the energy barriers of both the host matrix relaxations and of the long-range charge migration events characterizing the investigated electrolytes. These effects became more important as the temperature of the electrolytes is decreased going from III to I regions.

4. Conclusion

In this report, a family of magnesium-tin-based ionic liquid electrolytes for multivalent metal battery applications was developed. The accurate selection of the starting materials (*i.e.*, $Pyr_{14}Cl$ IL, Me_2SnCl_2 and δ-$MgCl_2$), allows to obtain electrolytes with extended coordination networks, where cation aggregates are neutralizing anion 3D catenated nanodomains. The thermal properties of the samples are strongly affected by the amount of δ-$MgCl_2$ doping of the electrolytes. The presence of the T_g, T_c, and T_m thermal transitions, and the dependence on $MgCl_x$ concentration of only T_c, and T_m, demonstrate that $MgCl_x$ species are embedded in extended anionic 3D catenated networks of electrolytes. Vibrational studies permit to discriminate the type of organochlorostannate repeat units involved in anionic domains of the ILs. In particular, by correlation methods and DFT calculations, in electrolytes it is proved the presence of $[Me_{2x}Sn_xCl_{2x+y}]^{y-}$ anionic repeat units, with $x = 1$ (monomer), 2 (dimer) and 3 (trimer). $MgCl_x$ species are coordinated by the organochlorostannate anionic repeat units, forming extended anionic 3D catenated networks where metal atoms (*i.e.*, Sn and Mg) are connected by means of chloride bridges. The ability of these electrolytes to deposit and strip a Mg–Sn metal alloy is demonstrated with cyclic voltammetry experiments, which indicate that the redox reactions occur with a very low overpotential with respect to those of similar electrolytes described in literature (<100 mV *vs.* Mg/Mg^{2+}). The presence of tin in the IL-based electrolytes thanks to its large difference in standard reduction potential with respect to magnesium is crucial in order to obtain alloy deposits rich in magnesium. The electric response and conduction mechanism of electrolytes are studied by means of broadband electrical spectroscopy. Results show that the electric response is dominated by several polarization phenomena, which confirm that in bulk electrolytes the typical heterogeneity is present, associated to the formation of the complex 3D anionic catenated networks and cation aggregates of Pyr_{14}^{+} stacks on the mesoscale. These mesoscale heterogeneities are responsible of the intricate network of conductivity pathways which concur to the overall conductivity of materials. At room temperature, an ionic conductivity of $1.19{\cdot}10^{-3}$ S cm^{-1} is achieved for the $[Pyr_{14}Cl/(Me_2SnCl_2)_{1.5}]/(\delta\text{-}MgCl_2)_{0.070}$ sample, which makes the proposed materials very promising for application in magnesium batteries. In addition, α and β dielectric relaxations are observed, whose frequency and intensity depend on T and on electrolyte composition. These events are assigned to the relaxation modes in nanodomains of the cation pyrrolidinium aggregates of stacks. Here, of crucial importance are α_1 and α_2 relaxations which are attributed to the diffusion of rotational states of Pyr_{14}^{+} units along the axis stacks. Indeed, polarization phenomena of conductivity pathways are effectively coupled with α dielectric relaxation events, stimulating efficiently the long-range charge migration processes in anionic 3D catenated magnesium-organochlorostannate networks of proposed IL electrolytes. Taken all together, the results here obtained allow to suggest that the conduction mechanism in the studied electrolytes consists in the exchange of electrochemically active metal species between neighboring delocalization bodies (DBs), σ_{EP}. In this case, DBs can be identified with the volume of the electrolyte including cationic and anionic catenated aggregates within which the charge carriers are exchanged so fast in the time scale of conductivity to be considered delocalized [63–65]. At medium and high temperatures, the presence of $MgCl_x$ species in the extended and complex anionic 3D catenated networks reduces the activation energy barrier of these processes. In summary, this study sheds light on the complexity of the coordination events and type of interactions which modulate the electrochemical performance of proposed IL electrolytes.

CRediT authorship contribution statement

Gioele Pagot: conceived the idea for the project and planned the experiments, completed, analyzed, Formal analysis, the vibrational spectroscopy investigations, Investigation, performed the electrochemical measurements and microscopy analyses on the electrodeposited alloy layer, executed the BES studies and elaborated the results, All the authors discussed the results, conceived the conclusions and contributed to the final version of the manuscript, Writing – original draft, drafted the manuscript with the support, Supervision. **Joy A. Kieser:** synthetized the electrolytes and performed the thermal analyses, Formal analysis, completed and analyzed the vibrational spectroscopy, Investigation, performed the electrochemical measurements and microscopy analyses on the electrodeposited alloy layer. **Federico Brombin:** synthetized the electrolytes and performed the thermal analyses, Formal analysis, completed and analyzed the vibrational spectroscopy, Investigation. **Keti Vezzù:** executed the BES studies and elaborated the results, All the authors discussed the results, conceived the conclusions and contributed to the final version of the manuscript. **Juergen Janek:** conceived the idea for the project and planned the experiments, Writing – original draft, drafted the manuscript with the support, Supervision. **Vito Di Noto:** conceived the idea for the project and planned the experiments, Writing – original draft, drafted the manuscript with the support, Supervision.

Declaration of competing interest

The authors declare that they have no known competing financial interests or personal relationships that could have appeared to influence the work reported in this paper.

Data availability

Data will be made available on request.

Acknowledgements

This work has been supported by the grant W911NF-21-1-0347 from the U.S. Army Research Office. JJ acknowledges funding within the POLIS Cluster of Excellence (funded by the DFG, Germany).

Appendix A. Supplementary data

Supplementary data to this article can be found online at https://doi.org/10.1016/j.jpowsour.2023.232910.

References

[1] R. Dominko, J. Bitenc, R. Berthelot, M. Gauthier, G. Pagot, V. Di Noto, Magnesium batteries: current picture and missing pieces of the puzzle, J. Power Sources 478 (2020), 229027, https://doi.org/10.1016/j.jpowsour.2020.229027.
[2] G. Pagot, K. Vezzù, A. Nale, M. Fauri, A. Migliori, V. Morandi, E. Negro, V. Di Noto, Chrysalis-like graphene oxide decorated vanadium-based nanoparticles: an

extremely high-power cathode for magnesium secondary batteries, J. Electrochem. Soc. 167 (2020), 070547, https://doi.org/10.1149/1945-7111/ab7fb4.
[3] E. Peled, D. Golodnitsky, H. Mazor, M. Goor, S. Avshalomov, Parameter analysis of a practical lithium- and sodium-air electric vehicle battery, J. Power Sources 196 (2011) 6835–6840, https://doi.org/10.1016/j.jpowsour.2010.09.104.
[4] J. Muldoon, C.B. Bucur, A.G. Oliver, T. Sugimoto, M. Matsui, H.S. Kim, G.D. Allred, J. Zajicek, Y. Kotani, Electrolyte roadblocks to a magnesium rechargeable battery, Energy Environ. Sci. 5 (2012) 5941, https://doi.org/10.1039/c2ee03029b.
[5] V. Di Noto, M. Fauri, Magnesium-based Primary (Non-rechargeable) and Secondary (Rechargeable) Batteries, 2001. WO 01/09972 A1. App. Number: PCT/EP00/07221, Priority: PD99A000179 of the 29 July 1999.
[6] M. York, K. Larson, K.C. Harris, E. Carmona, P. Albertus, R. Sharma, M. Noked, E. Strauss, H. Ragones, D. Golodnitsky, Recent advances in solid-state beyond lithium batteries, J. Solid State Electrochem. (2022), 05223, https://doi.org/10.1007/s10008-022-05223-w.
[7] D. Aurbach, Z. Lu, A. Schechter, Y. Gofer, H. Gizbar, R. Turgeman, Y. Cohen, M. Moshkovich, E. Levi, Prototype systems for rechargeable magnesium batteries, Nature 407 (2000) 724–727, https://doi.org/10.1038/35037553.
[8] F. Bertasi, K. Vezzù, G. Nawn, G. Pagot, V. Di Noto, Interplay between structure and conductivity in 1-Ethyl-3-methylimidazolium tetrafluoroborate/(δ-$MgCl_2$)$_f$ electrolytes for magnesium batteries, Electrochim. Acta 219 (2016) 152–162, https://doi.org/10.1016/j.electacta.2016.09.091.
[9] R. Mohtadi, O. Tutusaus, T.S. Arthur, Z. Zhao-Karger, M. Fichtner, The metamorphosis of rechargeable magnesium batteries, Joule 5 (2021) 581–617, https://doi.org/10.1016/j.joule.2020.12.021.
[10] J.D. Forero-Saboya, D.S. Tchitchekova, P. Johansson, M.R. Palacín, A. Ponrouch, Interfaces and interphases in Ca and Mg batteries, Adv. Mater. Interfac. 9 (2022), 2101578, https://doi.org/10.1002/admi.202101578.
[11] E. Peled, The electrochemical behavior of alkali and alkaline Earth metals in nonaqueous battery systems - the solid electrolyte interphase model, J. Electrochem. Soc. 126 (1979) 2047–2051, https://doi.org/10.1149/1.2128859.
[12] E. Peled, Film forming reaction at the lithium/electrolyte interface, J. Power Sources 9 (1983) 253–266, https://doi.org/10.1016/0378-7753(83)87026-8.
[13] E. Peled, C. Menachem, D. Bar-Tow, A. Melman, Improved graphite anode for lithium-ion batteries: chemically bonded solid electrolyte interface and nanochannel formation, J. Electrochem. Soc. 143 (1996), https://doi.org/10.1149/1.1836372. L4-L7.
[14] M.R. Busche, T. Drossel, T. Leichtweiss, D.A. Weber, M. Falk, M. Schneider, M. L. Reich, H. Sommer, P. Adelhelm, J. Janek, Dynamic formation of a solid-liquid electrolyte interphase and its consequences for hybrid-battery concepts, Nat. Chem. 8 (2016) 426–434, https://doi.org/10.1038/nchem.2470.
[15] H. El-Shinawi, A.S. Schulze, M. Neumeier, T. Leichtweiß, J. Janek, FeO_x-coated SnO_2 as an anode material for lithium ion batteries, J. Phys. Chem. C 118 (2014) 8818–8823, https://doi.org/10.1021/jp5016966.
[16] V. Di Noto, S. Lavina, D. Longo, M. Vidali, A novel electrolytic complex based on δ-$MgCl_2$ and poly(ethylen glycol) 400, Electrochim. Acta 43 (1998) 1225–1237, https://doi.org/10.1016/S0013-4686(97)10023-8.
[17] V. Di Noto, M. Vittadello, Mechanism of ionic conductivity in poly (ethylene glycol 400)/($MgCl_2$)$_x$ polymer electrolytes: studies based on electrical spectroscopy, Solid State Ionics 147 (2002) 309–316, https://doi.org/10.1016/S0167-2738(02)00016-4.
[18] A.R. Polu, R. Kumar, AC impedance and dielectric spectroscopic studies of Mg^{2+} ion conducting PVA–PEG blended polymer electrolytes, Bull. Mater. Sci. 34 (2011) 1063–1067, https://doi.org/10.1007/s12034-011-0132-2.
[19] R. Manjuladevi, S. Selvasekarapandian, M. Thamilselvan, R. Mangalam, S. Monisha, P.C. Selvin, A study on blend polymer electrolyte based on poly(vinyl alcohol)-poly (acrylonitrile) with magnesium nitrate for magnesium battery, Ionics 24 (2018) 3493–3506, https://doi.org/10.1007/s11581-018-2500-z.
[20] P. Canepa, S.-H. Bo, G. Sai Gautam, B. Key, W.D. Richards, T. Shi, Y. Tian, Y. Wang, J. Li, G. Ceder, High magnesium mobility in ternary spinel chalcogenides, Nat. Commun. 8 (2017) 1759, https://doi.org/10.1038/s41467-017-01772-1.
[21] S. Tamura, M. Yamane, Y. Hoshino, N. Imanaka, Highly conducting divalent Mg^{2+} cation solid electrolytes with well-ordered three-dimensional network structure, J. Solid State Chem. 235 (2016) 7–11, https://doi.org/10.1016/j.jssc.2015.12.008.
[22] B. Liang, V. Keshishian, S. Liu, E. Yi, D. Jia, Y. Zhou, J. Kieffer, B. Ye, R.M. Laine, Processing liquid-feed flame spray pyrolysis synthesized $Mg_{0.5}Ce_{0.2}Zr_{1.8}(PO_4)_3$ nanopowders to free standing thin films and pellets as potential electrolytes in all-solid-state Mg batteries, Electrochim. Acta 272 (2018) 144–153, https://doi.org/10.1016/j.electacta.2018.04.015.
[23] F. Bertasi, C. Hettige, F. Sepehr, X. Bogle, G. Pagot, K. Vezzù, E. Negro, S. J. Paddison, S.G. Greenbaum, M. Vittadello, A key concept in magnesium secondary battery electrolytes, ChemSusChem 8 (2015) 3069–3076, https://doi.org/10.1002/cssc.201500339.
[24] T.E. Sutto, T. Wong, J. Taft, T. Duncan, Mg^{2+} ion behavior in ionic liquids, ECS Trans. 25 (2010) 85–98, https://doi.org/10.1149/1.3414006.
[25] S. Jeremias, G.A. Giffin, A. Moretti, S. Jeong, S. Passerini, Mechanisms of magnesium ion transport in pyrrolidinium bis(trifluoromethanesulfonyl)imide-based ionic liquid electrolytes, J. Phys. Chem. C 118 (2014) 28361–28368, https://doi.org/10.1021/jp5071506.
[26] G.A. Giffin, A. Moretti, S. Jeong, S. Passerini, Complex nature of ionic coordination in magnesium ionic liquid-based electrolytes: solvates with mobile Mg^{2+} cations, J. Phys. Chem. C 118 (2014) 9966–9973, https://doi.org/10.1021/jp502354h.
[27] F. Bertasi, F. Sepehr, G. Pagot, S.J. Paddison, V. Di Noto, Toward a magnesium-iodine battery, Adv. Funct. Mater. 26 (2016) 4860–4865, https://doi.org/10.1002/adfm.201601448.
[28] G. Pagot, F. Bertasi, K. Vezzù, F. Sepehr, X. Luo, G. Nawn, E. Negro, S.J. Paddison, V.D. Noto, Three-dimensional catenated 1-ethyl-3-methylimidazolium halotitanate ionic liquid electrolytes for electrochemical applications, Electrochim. Acta 246 (2017) 914–923, https://doi.org/10.1016/j.electacta.2017.06.089.
[29] G. Pagot, K. Vezzù, S.G. Greenbaum, V. Di Noto, Hybrid twin-metal aluminum–magnesium electrolytes for rechargeable batteries, J. Power Sources 493 (2021), 229681, https://doi.org/10.1016/j.jpowsour.2021.229681.
[30] V. Di Noto, R. Zannetti, M. Viviani, C. Marega, A. Marigo, S. Bresadola, $MgCl_2$-supported Ziegler-Natta catalysts: a structural investigation by X-ray diffraction and Fourier-transform IR spectroscopy on thè chemical activation process through $MgCl_2$-ethanol adducts, Makromol. Chem. 193 (1992) 1653–1663, https://doi.org/10.1002/macp.1992.021930709.
[31] V. Di Noto, S. Bresadola, New synthesis of a highly active δ-$MgCl_2$ for $MgCl_2$/$TiCl_4$/$AlEt_3$ catalytic systems, Macromol. Chem. Phys. 197 (1996) 3827–3835, https://doi.org/10.1002/macp.1996.021971126.
[32] M. Vittadello, P.E. Stallworth, F.M. Alamgir, S. Suarez, S. Abbrent, C.M. Drain, V. Di Noto, S.G. Greenbaum, Polymeric δ-$MgCl_2$ nanoribbons, Inorg. Chim. Acta. 359 (2006) 2513–2518, https://doi.org/10.1016/j.ica.2006.01.044.
[33] G. Pagot, M. Garaga, A.L. Jadhav, L.F. O'Donnell, K. Vezzù, B. Itin, R.J. Messinger, S.G. Greenbaum, V. Di Noto, Interplay between coordination, dynamics, and conductivity mechanism in Mg/Al-catenated ionic liquid electrolytes, J. Power Sources 524 (2022), 231084, https://doi.org/10.1016/j.jpowsour.2022.231084.
[34] D.-T. Nguyen, S.-W. Song, Magnesium stannide as a high-capacity anode for magnesium-ion batteries, J. Power Sources 368 (2017) 11–17, https://doi.org/10.1016/j.jpowsour.2017.09.054.
[35] A.G. Davies, H.J. Milledge, D.C. Puxley, P.J. Smith, Crystal structure and Mössbauer spectrum of dimethyltin dichloride, J. Chem. Soc. Inorg. Phys. Theor. (1970) 2862–2866, https://doi.org/10.1039/J19700002862.
[36] M. Das, J. Buckle, P. Harrison, The far infra-red spectra and bonding of some five and six coordinate complex tin ions, Inorg. Chim. Acta. 6 (1972) 17–22, https://doi.org/10.1016/S0020-1693(00)91751-1.
[37] K.M. Dieter, C.J. Dymek, N.E. Heimer, J.W. Rovang, J.S. Wilkes, Ionic structure and interactions in 1-methyl-3-ethylimidazolium chloride-aluminum chloride molten salts, J. Am. Chem. Soc. 110 (1988) 2722–2726, https://doi.org/10.1021/ja00217a004.
[38] K. Matsumoto, R. Hagiwara, Z. Mazej, P. Benkič, B. Žemva, Crystal structures of frozen room temperature ionic liquids, 1-ethyl-3-methylimidazolium tetrafluoroborate ($EMImBF_4$), hexafluoroniobate ($EMImNbF_6$) and hexafluorotantalate ($EMImTaF_6$), determined by low-temperature X-ray diffraction, Solid State Sci. 8 (2006) 1250–1257, https://doi.org/10.1016/j.solidstatesciences.2005.12.018.
[39] V. Di Noto, E. Negro, J.-Y. Sanchez, C. Iojoiu, Structure-relaxation interplay of a new nanostructured membrane based on tetraethylammonium trifluoromethanesulfonate ionic liquid and neutralized nafion 117 for high-temperature fuel cells, J. Am. Chem. Soc. 132 (2010) 2183–2195, https://doi.org/10.1021/ja906975z.
[40] F. Bertasi, G. Pagot, K. Vezzù, A. Nale, G. Pace, Y. Herve Bang, G. Crivellaro, E. Negro, V. Di Noto, Lithiated nanoparticles doped with ionic liquids as quasi-solid electrolytes for lithium batteries, Electrochim. Acta 307 (2019) 51–63, https://doi.org/10.1016/j.electacta.2019.03.167.
[41] H. de Vries, S. Jeong, S. Passerini, Ternary polymer electrolytes incorporating pyrrolidinium-imide ionic liquids, RSC Adv. 5 (2015) 13598–13606, https://doi.org/10.1039/C4RA16070C.
[42] J. Adebahr, P. Johansson, P. Jacobsson, D.R. Macfarlane, M. Forsyth, Ab initio calculations, Raman and NMR investigation of the plastic crystal di-methyl pyrrolidinium iodide, Electrochim. Acta 48 (2003) 2283–2289, https://doi.org/10.1016/S0013-4686(03)00216-0.
[43] O.B. Babushkina, Phase behaviour and FTIR spectra of ionic liquids: the mixtures of 1-Butyl-1-methylpyrrolidinium chloride and $TaCl_5$, Z. Naturforsch.A 63 (2008) 66–72, https://doi.org/10.1515/zna-2008-1-212.
[44] B. Bednarska-Bolek, R. Jakubas, G. Bator, J. Baran, Vibrational study of the structural phase transition in bis (pyrrolidinium)-chloride-hexachloroantimonate (V) by infrared spectroscopy, J. Mol. Struct. 614 (2002) 151–157, https://doi.org/10.1016/S0022-2860(02)00235-1.
[45] W.F. Edgell, C. Ward, The Raman and infrared spectra of the series $(CH_3)_nSnCl_{(4-n)}$, J. Mol. Spectrosc. 8 (1962) 343–364, https://doi.org/10.1016/0022-2852(62)90036-X.
[46] J. Evans, J. Wahr, Thermodynamic and spectroscopic study of pyrrolidine. II. Vibrational spectra and configuration, J. Chem. Phys. 31 (1959) 655–662, https://doi.org/10.1063/1.1730442.
[47] G. Ramis, G. Busca, FTIR spectra of adsorbed n-butylamine, J. Mol. Struct. 193 (1989) 93–100, https://doi.org/10.1016/0022-2860(89)80124-3.
[48] D.L. Vien, N.B. Colthup, W.G. Fateley, G. GJ, The Handbook of Infrared and Raman Characteristic Frequencies of Organic Molecules, Academic Press Boston, San Diego, California, 1991.
[49] R. Okawara, D.E. Webster, E.G. Rochow, The infrared spectra of the methylacetoxysilanes and some methyltin carboxylates. The configuration of the trimethyltin and the dimethyltin cations, J. Am. Chem. Soc. 82 (1960) 3287–3290, https://doi.org/10.1021/ja01498a013.
[50] I. Beattie, F. Stokes, L. Alexander, Vibrational spectra of some chloro-and methylchloro-species of cadmium, indium, tin, antimony, tellurium, and iodine, J. Chem. Soc., Dalton Trans. (1973) 465–469, https://doi.org/10.1039/DT9730000465.
[51] M. Currie, J. Estager, P. Licence, S. Men, P. Nockemann, K.R. Seddon, M. Swadźba-Kwaśny, C. Terrade, Chlorostannate(II) ionic liquids: speciation, Lewis acidity, and

oxidative stability, Inorg. Chem. 52 (2013) 1710–1721, https://doi.org/10.1021/ic300241p.
[52] J.R. Ferraro, Other low-frequency vibrations, in: J.R. Ferraro (Ed.), Low-Frequency Vibrations of Inorganic and Coordination Compounds, Springer US, Boston, MA, 1971, pp. 267–277.
[53] V. Di Noto, D. Fregonese, A. Marigo, S. Bresadola, High yield $MgCl_2$-supported catalysts for propene polymerization: effects of ethyl propionate as internal donor on the activity and stereospecificity, Macromol. Chem. Phys. 199 (1998) 633–640, https://doi.org/10.1002/(SICI)1521-3935(19980401)199:4<633::AID-MACP633>3.0.CO;2-9.
[54] L. Esser, R. Macchieraldo, R. Elfgen, M. Sieland, B.M. Smarsly, B. Kirchner, $TiCl_4$ dissolved in ionic liquid mixtures from Ab initio molecular dynamics simulations, Molecules 26 (2021) 79, https://doi.org/10.3390/molecules26010079.
[55] V. Di Noto, G.A. Giffin, K. Vezzù, M. Piga, S. Lavina, Broadband dielectric spectroscopy: a powerful tool for the determination of charge transfer mechanisms in ion conductors, in: Solid State Proton Conductors, 2012, pp. 109–183.
[56] K. Kobayashi, G. Pagot, K. Vezzù, F. Bertasi, V. Di Noto, Y. Tominaga, Effect of plasticizer on the ion-conductive and dielectric behavior of poly(ethylene carbonate)-based Li electrolytes, Polym. J. 53 (2021) 149–155, https://doi.org/10.1038/s41428-020-00397-4.
[57] T. Furukawa, M. Imura, H. Yuruzume, Broad-band conductive spectra of polypropylene oxide complexed with $LiClO_4$, Jpn. J. Appl. Phys. 36 (1997) 1119–1125, https://doi.org/10.1143/JJAP.36.1119.
[58] S.U. Vallerien, F. Kremer, C. Boeffel, Broadband dielectric spectroscopy on side group liquid crystal polymers, Liq. Cryst. 4 (1989) 79–86, https://doi.org/10.1080/02678298908028960.
[59] F. Fan, Y. Wang, T. Hong, M.F. Heres, T. Saito, A.P. Sokolov, Ion conduction in polymerized ionic liquids with different pendant groups, Macromolecules 48 (2015) 4461–4470, https://doi.org/10.1021/acs.macromol.5b00257.
[60] G. Pagot, S. Tonello, K. Vezzù, V. Di Noto, A new glass-forming electrolyte based on lithium glycerolate, Batteries 4 (2018) 41, https://doi.org/10.3390/batteries4030041.
[61] G. Pagot, F. Bertasi, G. Nawn, E. Negro, A. Bach Delpeuch, K. Vezzù, D. Cristofori, V. Di Noto, Effect of graphite and copper oxide on the performance of high potential $Li[Fe_{1/3}Ni_{1/3}Co_{1/3}]PO_4$ olivine cathodes for lithium batteries, Electrochim. Acta 225 (2017) 533–542, https://doi.org/10.1016/j.electacta.2016.12.149.
[62] G. Tammann, W. Hesse, Die Abhängigkeit der Viscosität von der Temperatur bie unterkühlten Flüssigkeiten, Z. Anorg. Allg. Chem. 156 (1926) 245–257, https://doi.org/10.1002/zaac.19261560121.
[63] G.A. Giffin, G.M. Haugen, S.J. Hamrock, V. Di Noto, Interplay between structure and relaxations in perfluorosulfonic acid proton conducting membranes, J. Am. Chem. Soc. 135 (2013) 822–834, https://doi.org/10.1021/ja3099799.
[64] K. Vezzù, G. Nawn, G. Pagot, E. Negro, A. Nale, Y.H. Bang, F. Conti, G. Cavinato, V. Di Noto, Relaxation phenomena and conductivity mechanisms in anion-exchange membranes derived from polyketone, Electrochim. Acta 319 (2019) 253–263, https://doi.org/10.1016/j.electacta.2019.06.139.
[65] G. Nawn, K. Vezzù, F. Bertasi, G. Pagot, G. Pace, F. Conti, E. Negro, V. Di Noto, Electric response and conductivity mechanism in H_3PO_4-doped polybenzimidazole-4N−HfO_2 nanocomposite membranes for high temperature fuel cells, Electrochim. Acta 228 (2017) 562–574, https://doi.org/10.1016/j.electacta.2016.12.151.